ChemPhotoChem

Research Article
doi.org/10.1002/cptc.202400343

Chemistry Europe
European Chemical Societies Publishing

www.chemphotochem.org

Photocatalytic Activity and Stability of Carbon Nitride-Pyrite Composites

Julian Kaulbersch,[a] Scott McGuigan,[b] Jana Timm,[a] Paul Maggard,[b] and Roland Marschall*[a]

In photocatalysis, the photoabsorber plays a crucial role in the reaction. The most important parameters are stability, cost and optical band gap. In this work, a prominent class of absorbers, namely carbon nitrides (CN), has been investigated. In the literature, CN is most often described as stable, although photodegradation has been observed. In order to retain the beneficial properties of CN while improving stability, a crystalline phase poly(triazine imide) (PTI) of carbon nitride was investigated and compared to polymeric CN in photocatalytic hydrogen generation experiments. In order to improve the charge separation for the photoinduced hydrogen evolution reaction, pyrite (FeS_2) was used as a surface co-catalyst with a loading of 1, 5 and 10 wt%. At the same time, any photodegradation products in solution were investigated by ion chromatography. Interestingly, PTI shows hardly any photocorrosion compared to defective carbon nitride, indicating its higher photostability in hydrogen evolution experiments. However, FeS_2 produces ammonium as a degradation product when synthesised from nitrogen-containing precursors. When made from nitrogen-free precursors, FeS_2 together with photostable PTI releases little ammonia, making it a photostable, earth-abundant composite for photocatalytic hydrogen generation.

Introduction

Global warming is one of the most serious problems facing humanity today. Most of the environmental problems are caused by humans through deforestation, energy extraction and use of fossil fuels, and agricultural practices,[1] with immense environmental, social and economic impacts.[2] It is therefore a major problem because it affects society, the economy and the environment. The production of greenhouse gases is directly proportional to the rate of global warming. Therefore, greenhouse gas emissions and adaptation to climate change need to be addressed simultaneously. More efficient energy use is one way to reduce greenhouse gas emissions, and there is a clear need for technologies to successfully convert and store the intermittent renewable energy generated by wind turbines or photovoltaics. At the same time, global energy demand is growing steadily at an average of 1–2% per year.[3]

Solar energy can be converted into electricity or chemical energy in a number of ways. As a high-energy molecule, hydrogen is a potential alternative to fossil fuels. Most hydrogen today is produced by a process called steam reforming, which relies heavily on fossil fuels. However, a cleaner method of producing hydrogen could be through the use of renewable energy, in particular the electrolysis of water to produce hydrogen.[4,5] However, electrolysis involves two production steps that have a negative impact on the overall process. One possible replacement is the process of solar fuel and hydrogen production using photocatalysis, which converts sunlight directly into the desired product on the surface of semiconductor materials.[6]

One of these is the promising material class of carbon nitrides (CNs) as a photo-absorber. As an n-type semiconductor, CN exhibits promising properties due to its band gap of ~2.7 eV and its composition of earth-abundant materials.[7–9] CN is typically synthesized by thermal polymerization of organic precursors such as urea, melamine or cyanamide. Polymerization conditions and precursors affect its structure and properties by influencing defect concentration, degree of polymerization, optical band gap and surface area. A common strategy used to enhance the activity of CN is the introduction of nitrogen vacancies. These vacancies act as effective adsorption and activation centers, thereby enhancing the photocatalytic performance of CN.[7] These factors appeared to enhance the nitrogen reduction reaction (NRR) in photocatalysis. However, recent evidence suggests that these vacancies lead to self-degradation during the photocatalytic process. This raises questions about the reported high NRR performance and suggests that the observed effects may be due to self-degradation of the system rather than true catalytic activity.[10] In order to reduce self-degradation and improve the hydrogen evolution reaction (HER), a bio-inspired[11] composite with iron sulphide, namely pyrite (FeS_2), was developed. However, this composite did not increase the stability due to charge

[a] J. Kaulbersch, J. Timm, R. Marschall
University of Bayreuth, 95440 Bayreuth, Germany
E-mail: roland.marschall@uni-bayreuth.de

[b] S. McGuigan, P. Maggard
Department of Chemistry and Biochemistry, Baylor University, Waco, TX 76798, USA

Supporting information for this article is available on the WWW under https://doi.org/10.1002/cptc.202400343

separation as expected, but reduced the CN stability even more.[10]

A possible solution to this degradation is a more crystalline phase of CN with improved stability. There are several unique types of CN with individual structural and functional properties. Most carbon nitrides inhabit the basic triazine (C_3N_3) and tri-s-triazine/heptazine (C_6N_7) units shown in Figure 1. The most prominent is the graphitic CN mentioned above, which consists of heptazine units. This material is very popular because of its wide range of applications.[13] Other interesting phases of carbon nitride include β-C_3N_4, which is predicted to have high hardness. Its structure is a three-dimensional network formed by sp^3 hybridized carbon atoms bonded to trigonal planar nitrogen. With exceptional mechanical properties, it is a candidate for high performance applications.[14] The structurally related α-C_3N_4 phase is another 3D structure composed of sp^3-hybridized carbon. It is hypothesized to have remarkable mechanical properties similar to β-C_3N_4.[15] Both phases have suitable optical properties for photocatalytic hydrogen evolution, low density, high chemical resistance and thermal stability, making them an interesting alternative to their well-known competitors. One of their disadvantages is the complicated synthesis, which is usually achieved by synthesizing coatings.[16] One emerging candidate of this material class is poly(triazine imide) (PTI). The concept of increasing the stability of material by crystallization of ordered structures is applied here. The structural order was achieved by intercalation of lithium and chlorine ions into the structure, resulting in a well-defined structure.[17] In contrast to these 3D-structured phases, various amorphous phases of CN exist, such as the amorphous CN (a-CN_x). These amorphous CN phases lack long-range order compared to the 3D-structured phases. On the other hand, these a-CN_x are highly tunable by varying the ratio of carbon to nitrogen. Thus, electrical conductivity, optical transparency and mechanical hardness can be tuned.[18,19] In addition, porous CN (p-C_3N_4) consists of s-triazine or tri-s-triazine polymer units. To increase catalytic activity, porous CN can be introduced by etching to increase the surface area of the material. However, the increased porosity does not always have the desired effect.[20] N-doped carbon nitrides introduce nitrogen doping for improved catalytic performance in several applications. For example, C_3N_5 exhibits semiconductor behavior with a narrow band gap. The narrowing of the band gap is due to the high nitrogen content, which changes the conduction and valence band positions. This results in enhanced carrier mobility and improved photocatalytic efficiency.[7,21] With all the different phases, CN shows a remarkable phase diversity. The different structures and properties with amorphous and crystalline phases show great promise in catalytic applications and other possible implementations in everyday use, such as energy storage or engineering.[12]

In this work, we used poly(triazine imide) (PTI), which consists of a crystalline phase of CN with lithium and chloride ions intercalated in the structure,[17] as a photoabsorber for photocatalytic hydrogen evolution, and compared it with polymeric, vacancy-rich CN (V_N-CN), to demonstrate the photostability of PTI in contrast to amorphous V_N-CN. To enhance the photocatalytic activity, both materials were modified with the earth-abundant FeS_2 as a co-catalyst. The hydrogen evolution activity and stability of the different CNs with FeS_2 were investigated in an argon atmosphere, and ion chromatography was used to analyze any photodegradation. In these photocatalytic experiments, we can confirm that PTI is not photocorrosive releasing hardly any ammonia, in contrast to V_N-CN. We also show that the choice of nitrogen-containing precursors for the synthesis of inorganic catalysts such as FeS_2 can clearly lead to false-positive ammonia detection results, which needs to be addressed by the community.

Results and Discussion

Material Synthesis & Characterization

The structural analysis of the carbon nitrides, pyrites (FeS_2) and composites was first performed by X-ray diffraction (XRD). The XRD pattern of vacancy-rich carbon nitride (V_N-CN) shown in Figure 2 exhibits the typical two broad reflections at 13° and 27.4° 2θ, where the reflections can be attributed to in-plane and interplanar stacking, respectively.[7] The heptazine units are created through thermal polymerisation, forming a structure with hydrogen bridges at their edges. This structure is

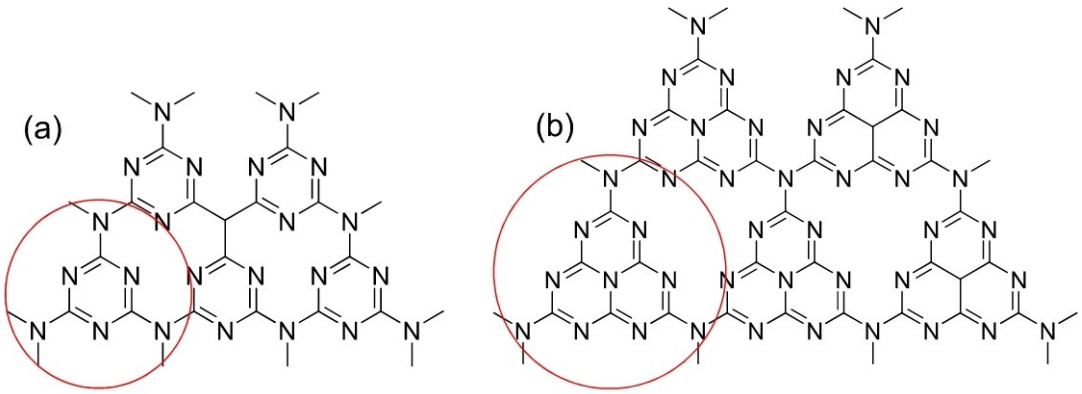

Figure 1. The triazine (a) and heptazine (b) structures and units of the different carbon nitrides.[12]

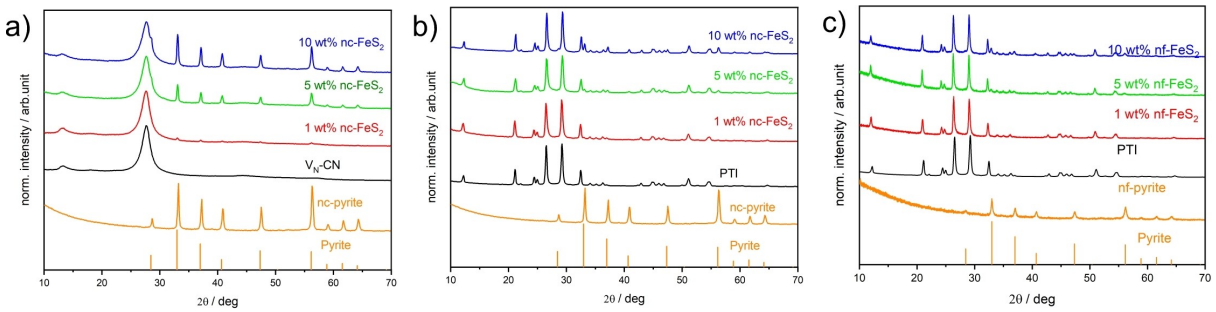

Figure 2. Powder XRD patterns for V_N-CN with nc-pyrite a), PTI with nc-pyrite b), and PTI with nf-pyrite c). In a) the pure nc-FeS_2 and pure V_N-CN are shown. Furthermore, the nc-FeS_2 loading of 10, 5 and 1 wt% loading on V_N-CN is shown. In b) the pure nc-FeS_2 and pure PTI are shown. The nc-FeS_2 loading of 10, 5 and 1 wt% loading on PTI is shown. In c) the pure nf-FeS_2 and pure PTI are shown with the nf-FeS_2 loading of 10, 5 and 1 wt% loading on PTI.

analogous to interconnected melon chains with an orthorhombic space group,[22] suggesting a different C/N ratio than the presumed 3:4 ratio of stoichiometric C_3N_4. The crystalline PTI shows defined and narrow reflections in the XRD pattern.[17] The synthesis of FeS_2 with a nitrogen-containing precursor (nc-FeS_2) and a nitrogen-free precursor (nf-FeS_2) resulted in the formation of materials with both phase purity (Figure 2). The intensity and broadening of the reflections vary between the two samples, indicating that the synthesis route involving a nitrogen-containing precursor (thiourea) results in the formation of more crystalline products.

The X-ray diffraction patterns of the composites display reflections characteristic of V_N-CN or PTI as well as FeS_2, so the successful formation of composites is confirmed. No additional phase was observed in the XRD patterns.

The intensity of the reflections originating from FeS_2 increases with the increasing amount of FeS_2 in the composites, demonstrating the successful synthesis of composites with different ratios of nc-FeS_2 to V_N-CN, nc-FeS_2 to PTI and nf-FeS_2 to PTI. Furthermore, the different ratios in the composites were discernible through a change in colour. This was due to the black colour of the iron sulphides, the light yellow colour of V_N-CN and the beige to white colour of PTI (Figure S1).

The morphologies of the different composites were investigated through the utilisation of scanning electron microscopy (SEM) images and energy-dispersive X-ray (EDX) mapping. Figure 3 presents scanning electron microscopy (SEM) images and energy-dispersive X-ray spectroscopy (EDX) mapping of the V_N-CN composite with 10 wt% loading of nc-FeS_2. While the contrast between the V_N-CN and nc-FeS_2 is not particularly pronounced, the EDX mapping clearly demonstrates the extent to which the surface of the V_N-CN is covered by nc-FeS_2. Moreover, the spherical shape and agglomerate formation of nc-FeS_2 and nf-FeS_2 (Figure S2) are in accordance with the EDX mapping results. The SEM image of the nc-FeS_2 particles reveals that their size is approximately 50–80 nm, with a tendency to cluster into larger agglomerates, measuring 300–400 nm. A comparable phenomenon can be observed in the case of the

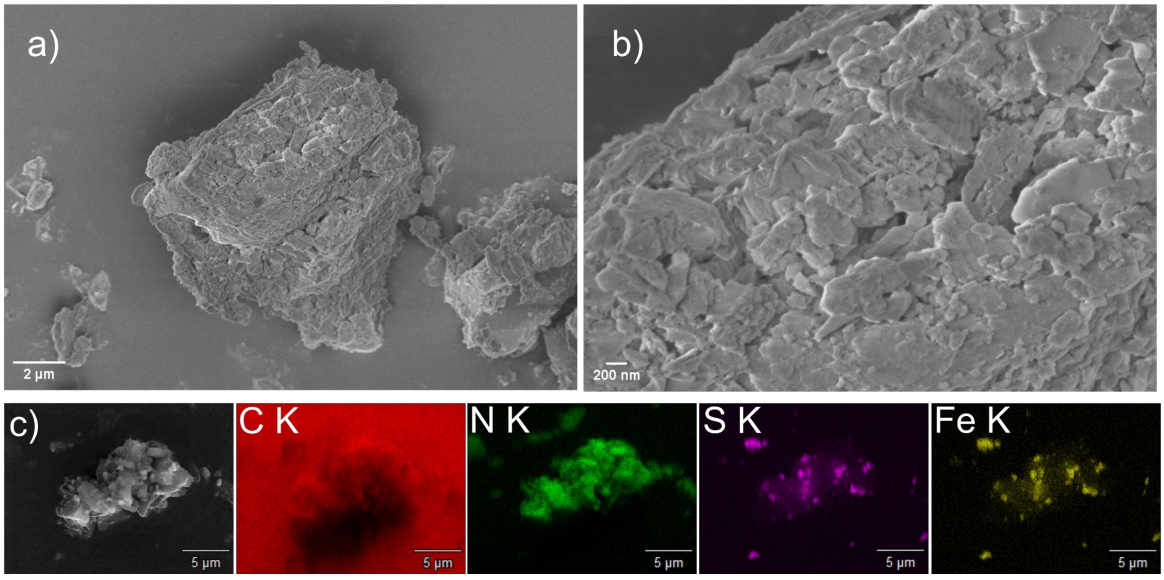

Figure 3. The SEM images show the 10 wt% loading of nc-FeS_2 on the V_N-CN. In image a) an overview of a particle is shown. The distribution of FeS_2 on the V_N-CN background can be observed in image b). EDX analysis was conducted and confirmed the FeS_2 particles are contributed on the V_N-CN surface shown in image c).

nf-FeS_2, where the individual particles are smaller, measuring between 35 and 50 nm, yet larger agglomerates, spanning a range of 350–660 nm, are present. With regard to PTI and its composites, the SEM images illustrate the morphology of agglomerated rod-like crystals for pure PTI (Figure S3). Similarly, the EDX mapping of PTI composites with 10% loading of nc-FeS_2 (Figure S4) and with 10% loading of nf-FeS_2 (Figure S5) revealed comparable observations to those made for VN-CN, namely, a notable surface coverage of PTI.

To provide further evidence of the presence of FeS_2 in the composite materials, transmission electron microscopy (TEM) images were collected. As illustrated in Figure S6, the TEM images provide insight into the lattice planes of the various materials. Given the amorphous nature of V_N-CN, no lattice planes were discernible in the TEM. In contrast, the nc-FeS_2 exhibits the (121) lattice plane with a spacing of 2.1 Å, whereas the nf-FeS_2 displays the (021) lattice plane with 2.5 Å. These observations align with the results of our calculations based on a crystallographic information file (cif),[23] further substantiating the presence and phase purity of pyrite, FeS_2. In the composite comprising 10 wt% FeS_2 on V_N-CN, the (111) lattice plane with a spacing of 3.1 Å and the (021) lattice plane with a spacing of 2.4 Å of FeS_2 can be discerned. The amorphous nature of V_N-CN makes it challenging to resolve the lattice planes in this instance. Upon examination of the 10 wt% nc-FeS_2 on PTI, the (021) lattice plane of FeS_2 and the (200) plane of PTI with a spacing of 3.3 Å could be observed. This evidence unequivocally demonstrates that the two materials are in contact. A comparable observation is made for the 10 wt% nf-FeS_2 on PTI, where the (021) lattice plane of FeS_2 with a spacing of 2.4 Å and the (200) plane of PTI with a spacing of 3.4 Å confirm the presence of both materials.

In order to ascertain the defined optical properties, the materials were subjected to characterisation by means of absorption spectroscopy in diffuse reflectance. CN is an indirect, n-type semiconductor.[7–9] Therefore, an indirect Tauc plot was used to determine the band gap.[24] The Kubelka-Munk plots[25] (Figure 4) were also constructed to compare the determined Tauc plots. The band gap from Tauc plots of V_N-CN is 2.71 eV (Figure S7) and is in good accordance to the literature.[10] All V_N-CN composites display comparable band gaps. This is anticipated due to the concentration ratios inherent to the composites, and thus the impact of the absorption cannot be attributed to FeS_2; consequently, it will not be subjected to detailed examination. Nevertheless, the band gap increased during the formation of the composite, rising from 2.71 eV up to 2.77 eV in comparison to bare V_N-CN. These observations suggest alterations in the electronic structure and the accessibility of electrons within the π-system.[10] The V_N-CN composite with 10 wt% FeS_2 exhibits the highest absorption, which may be indicative of an altered electronic structure of the composite. In accordance with its colour, PTI exhibits a larger band gap of 3.12 eV. In this context, it would appear that the addition of FeS_2 does not result in any significant alteration to the electrical properties of PTI, as the band gap remains at approximately 3.13 eV, indicating a virtually unchanged state (cf. Figure S1). This may be attributed to the pre-existing structural alterations induced by the intercalated LiCl, which appears to exert a more pronounced influence on the electronic structure. The band gaps obtained from the Kubelka–Munk and Tauc plots (Figure 4 and Figure S7) are presented in Supporting Information Table S1 for reference.

In order to ascertain the functional groups of the materials, diffuse reflectance infrared Fourier transform (DRIFT) spectra were collected (Figure 5). The broad signal observed between 3000 and 3600 cm^{-1} can be attributed primarily to N–H stretching vibrations,[26] which are present in the non-ideal CN structure. This provides further confirmation of the existence of free amino groups resulting from incomplete thermal polymerisation. The stretching modes of C=N and C–N can be assigned to the sharp peaks between 1700 and 1200 cm^{-1}, as observed in the heterostructure and in the bridge of the heptazine units. This is in accordance with the findings in literature.[27–29] The aforementioned cyano groups are evident at 2150 cm^{-1}, thereby corroborating the presence of structural imperfections. The spectra of the composites are comparable to those of V_N-CN, indicating the maintenance of the structural integrity. The signals for heterocycle vibrations at higher wavenumbers (approximately 1700 cm^{-1}) originate from C=N vibrations, while those at lower wavenumbers (approximately 1100 cm^{-1}) are attributed to C–N vibrations.[30] As observed in previous work, the addition of FeS_2 affects the C=N vibrations, as does the slight shift of the heptazine unit vibrations to lower wavenumbers. This is due to small changes in the vibrational energy of the entire heptazine framework.[10] PTI shows a similar DRIFT spectrum to that of V_N-CN. It has two sharp signals which

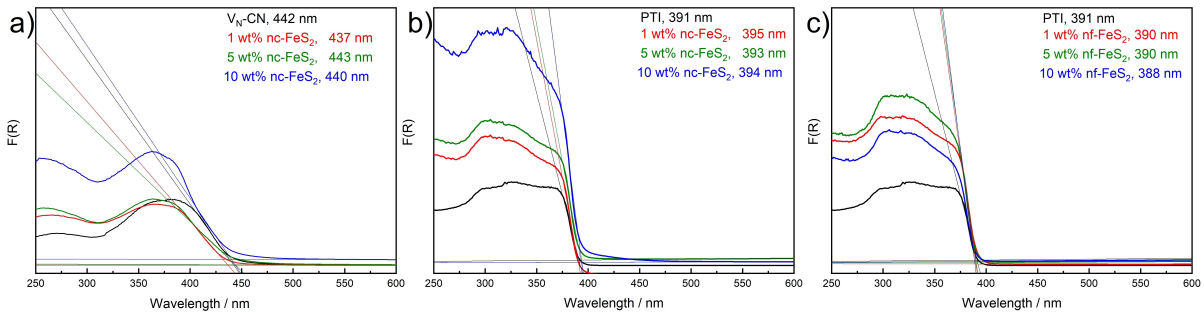

Figure 4. Kubelka–Munk plots for the bare V_N-CN with 1, 5 and 10 wt% loading of nc-FeS_2 a), the bare PTI with 1, 5 and 10 wt% loading of nc-FeS_2 b), and bare PTI with 1, 5 and 10 wt% loading of nf-FeS_2 are plotted c).

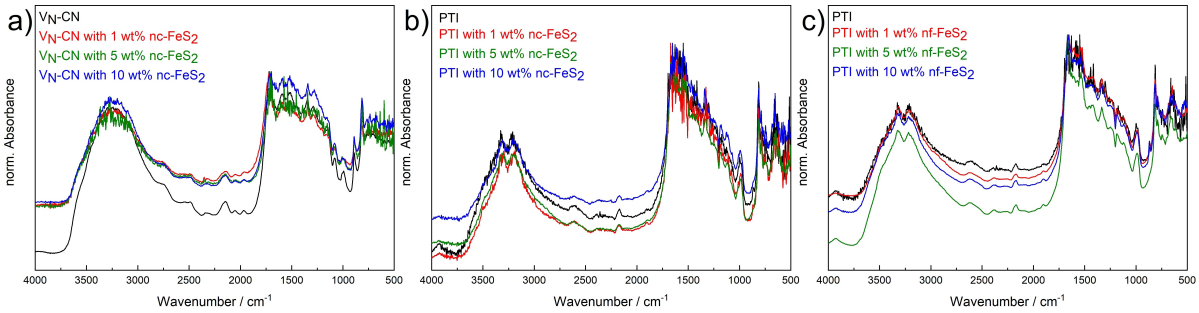

Figure 5. DRIFT spectra of the bare V_N-CN with 1, 5 and 10 wt% loading of nc-FeS_2 a), the bare PTI with 1, 5 and 10 wt% loading of nc-FeS_2 b), and bare PTI with 1, 5 and 10 wt% loading of nf-FeS_2 are plotted c).

overlay with very broad N–H/O–H signals between 3000 and 3600 cm^{-1}. The two signals observed at 3327 and 3213 cm^{-1} can be attributed to the N–H stretching band.[31] Additionally, the spectra exhibit evidence of cyano groups at 2175 cm^{-1}. No discernible alterations are evident in the PTI/FeS_2 composites when compared to the pure PTI. This corroborates the findings of the absorption spectroscopy, which also demonstrated no alterations subsequent to the formation of the composite.

The efficiency of a photocatalyst is defined in terms of its capacity to absorb light and subsequently convert photons into charge carriers. The most commonly employed method for acquiring data regarding the energy relaxation energy levels is photoluminescence (PL) spectroscopy. In semiconductors, a variety of emission signals are possible, with the most prominent PL emission typically resulting from band gap emission. In this process, the carriers recombine and relax to the ground state by emitting radiation. Consequently, the PL emission intensity is frequently employed as a criterion for the evaluation of carrier separation and recombination rates. In general, a reduction in PL signal intensity is indicative of a reduction in recombination rate and an improvement in carrier separation. CN exhibits a striking blue fluorescence, while defects in CN exert a pronounced influence on the PL emission signals.[32] At an excitation wavelength of 355 nm, all materials exhibit a broad fluorescence signal between 400 and 620 nm, with an emission maximum at 459 nm (V_N-CN) and at 435 nm (PTI), as illustrated in Figure 6. The difference in PL intensity between V_N-CN-based and PTI-based materials is significant, demonstrating that PTI materials exhibit minimal PL emission. Following the formation of the composite, a reduction in PL intensity was observed for all composite materials in comparison to the respective bare V_N-CN and PTI materials. This may lead to the assumption that the carrier recombination is diminished; however, another factor to consider is the dilution of the luminescent material, V_N-CN, with the non-luminescent material, FeS_2. Furthermore, the observed trend of decreasing PL intensities with increasing amounts of FeS_2 in the composites is not fully consistent. This phenomenon may be attributed to the statistical and random distribution of FeS_2 on the surface of V_N-CN and PTI, as observed in the scanning electron microscopy (SEM) and transmission electron microscopy (TEM) images in Figures 3 and Figure S2–S6, respectively. Consequently, it is plausible that in the reflection measuring mode, an area with varying degrees of non-luminescent FeS_2 may be exposed. In light of these uncertainties in the interpretation of the absolute PL values, it is evident that the quantum yield (QY) is a superior indicator of the carrier recombination rates. Table 1 presents the quantum yield values for all samples.

The quantum yield (QY) values indicate that PTI exhibits a lower degree of fluorescence in comparison to V_N-CN. Consequently, the calculation and interpretation of the QY for the PTI-containing samples is considerably more challenging than for V_N-CN. As anticipated, the decrease in QY values with increasing FeS_2 content in the composites is in accordance with previous findings,[10] indicating a reduction in radiative recombination of charge carriers.

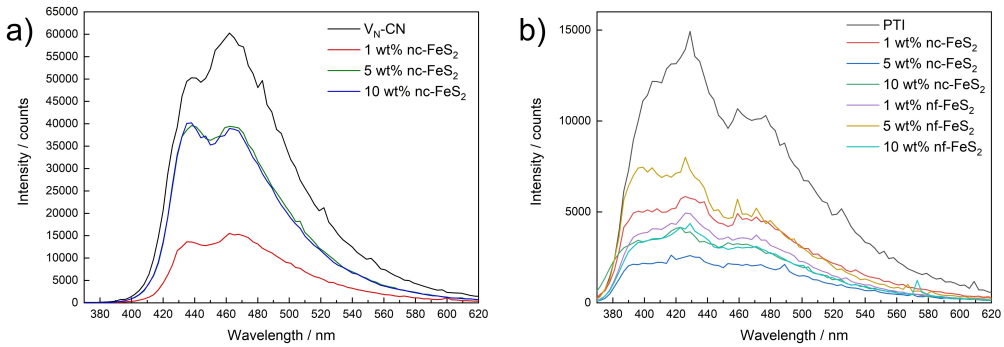

Figure 6. PL of the bare V_N-CN and the composites with 1, 5 and 10 wt% nc-FeS_2 a), the PTI and the composites with 1, 5 and 10 wt% nc-FeS_2 and with 1, 5 and 10 wt% nf-FeS_2 are shown in b).

Table 1. Quantum yield of all sample. Excitation wavelength 355 nm and detection at each respective PL maximum.

Sample	V_N-CN	1 wt% nc-FeS_2 on V_N-CN	5 wt% nc-FeS_2 on V_N-CN	10 wt% nc-FeS_2 on V_N-CN
Quantum yield	12.1%	7.2%	7.9%	6.5%
Sample	PTI	1 wt% nc-FeS_2 on PTI	5 wt% nc-FeS_2 on PTI	10 wt% nc-FeS_2 on PTI
Quantum yield	2.2%	1.5%	4.0%	0.9%
Sample		1 wt% nf-FeS2 on PTI	5 wt% nf-FeS2 on PTI	10 wt% nf-FeS2 on PTI
Quantum yield		2%	5.3%	2.1%

In the case of V_N-CN based materials, the intensity of the normalised PL spectrum (Figure S8) of the emission at 435 nm is markedly elevated in comparison to that at 459 nm in the composites. In the case of PTI-based materials, the signal at approximately 400 nm is more pronounced. Based on the absorption spectroscopy data presented in Figure 4, the PL emission signals at 435 nm and 400 nm (for materials based on V_N-CN and PTI) can be attributed to direct band gap emission. In contrast, the PL emission signals at 459 nm and 430 nm originate from electronic state transitions within the band gap, involving lone electron pairs at N–$(C)_3$ sites. It is possible that the observed tail is the result of defects, which could lead to emissions at higher wavelengths. The observed PL emission signals can be attributed to transitions from various states within the material, including lone pair states of nitrogen atoms in the s-triazine moiety, amino groups, NH-bridging moieties, and potentially graphitic regions.[33,34] The markedly diminished PL intensities at 459 nm and 430 nm suggest a reduction in radiative recombination at these lone electron pairs and defects. It can therefore be surmised that V_N-CN, PTI and FeS_2 interact via the N–$(C)_3$ groups, thereby modifying the electronic structure of the composites in comparison to the properties of the materials in their unmodified state. It is possible that the charge transfer may contribute to exciton separation and delayed recombination.

The radiative carrier recombination rates were analysed by measuring the PL lifetimes using time-correlated single photon counting (TCSPC). The PL lifetime can be fitted by three exponential functions due to the assignment of different overlapping PL signals within the respective PL emission signal. Given the similarity of their structural models, it is reasonable to conclude that V_N-CN and PTI will exhibit comparable PL recombination processes. It can therefore be surmised that the PL lifetime τ_1 is attributable to interlayer carrier recombination (along the π-stacking direction), τ_2 to intraplanar and intrachain carrier recombination, and τ_3 to carrier recombination within the aromatic system.[8,35] The PL lifetimes of all samples are presented in Table S2 for reference. Excitation at 355 nm was employed, with the PL detection wavelength set to the respective local PL maximum. The shortest τ_3 lifetimes are observed for all samples, with slight variations in the range of 0.4–1 ns for V_N-CN-based materials and 0.1–0.5 ns for PTI-based materials. A comparison of the bare V_N-CN and PTI with their composites reveals that the τ_3 lifetimes remain within the same range, which suggests that the electronic structure of the aromatic system remains unaltered due to the formation of the composite. With regard to the time constant τ_2, the values observed for V_N-CN and its composites exhibit a range of 2.1 ns to 4.6 ns, with the PL emission at 467 nm demonstrating the most notable discrepancy for τ_2, at 4.1 ns. It was observed that the PL lifetime increased in proportion to the quantity of FeS_2 present. This variation in the PL lifetime highlights a change in the polarisation of the heptazine framework, which consequently affects the electronic structure of the heptazine framework due to composite formation. As with V_N-CN and its composites, the τ_2 lifetimes of PTI and its composites are also altered by the formation of the composites. However, the range of values is less pronounced, and the trend observed for VN-CN and its composites is reversed, with an increase in FeS_2 amount resulting in a slight decrease in PL lifetime. It may be reasonably assumed that PTI and its composites will exhibit a similar trend to that observed for V_N-CN and its composites with regard to the PL emission at 468 nm. With regard to the time constant τ_1, it is evident that the changes observed in V_N-CN and its composites are considerably more pronounced in comparison to those observed in PTI and its composites. The values of time constant τ_1 for V_N-CN and its composites demonstrate an increase with rising FeS_2 content (467 nm emission), whereas for PTI and its composites, the values of τ_1 exhibit a decrease with rising FeS_2 concentration for PL emission at 405 nm and an increase with rising FeS_2 concentration for PL emission at 468 nm. The TCSPC data demonstrate that the carrier recombination dynamics of both materials are altered following the formation of composites, with changes observed in intra- and interchain recombination, as well as interlayer recombination (along the π-stacking direction). The primary distinction between the materials lies in the impact of these alterations. In the case of V_N-CN, it appears that the formation of composites facilitates the recombination of carriers, whereas in PTI composites, the excited state of carriers appears to be stabilised.

X-ray photoelectron spectroscopy (XPS) was conducted on the following samples: 10 wt% nc-FeS_2 on V_N-CN, PTI, 10 wt% nc-FeS_2 on PTI, 10 wt% nf-FeS_2 on PTI, nc-FeS_2, and nf-FeS_2. The XP survey spectra confirm the presence of the anticipated elements in each sample (Figure 7). It is noteworthy that the peaks observed in the XP spectra of the two forms of FeS_2 are similar. It is therefore surprising that nitrogen cannot be

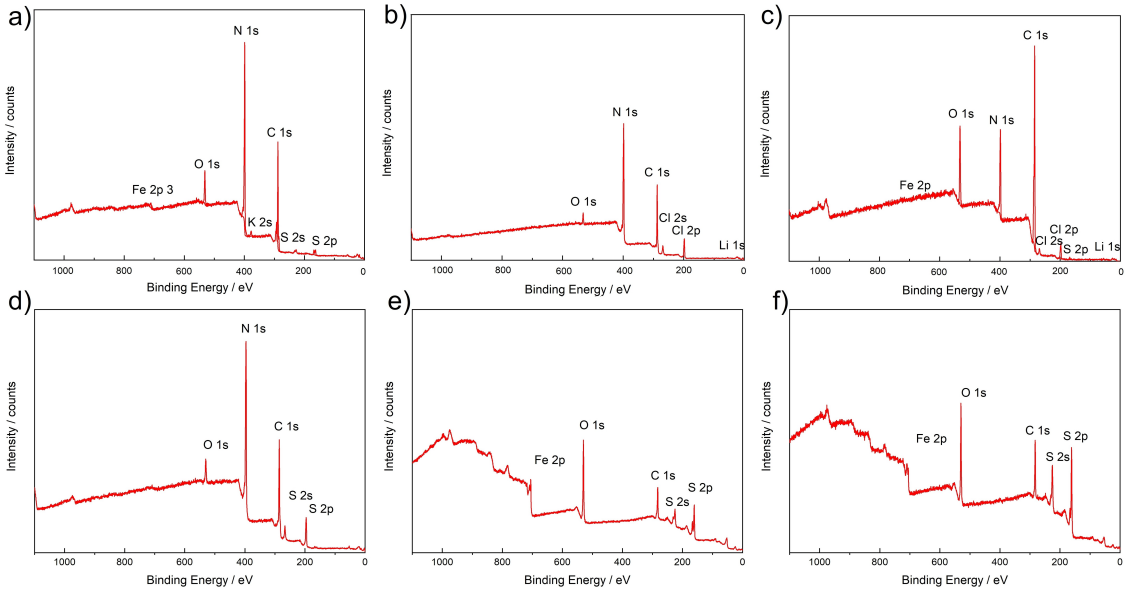

Figure 7. XP survey spectra of 10 wt% nc-FeS_2 on V_N-CN a), PTI b), 10 wt% nc-FeS_2 on PTI c), 10 wt% nf-FeS_2 on PTI d), nc-FeS_2 e) and nf-FeS_2 f) with the respective assignment of the elements.

detected, despite the use of nitrogen-containing precursors for the synthesis of nc-FeS_2. In order to gain further insight, core-level spectra of 10 wt% nc-FeS_2 on PTI and 10 wt% nf-FeS_2 on PTI were recorded and analysed in greater detail. Given the structural similarities between the two pure materials (V_N-CN and PTI), the target carbon-to-nitrogen (C:N) ratio is typically around 3:4.[17,36] Nevertheless, the analysis indicated a C:N ratio of 4:5, which could be attributed to adventitious carbon or a reduced surface nitrogen content. The PTI with 10 wt% nc-FeS_2 exhibited a C:N ratio of approximately 3:1, indicating an increase in carbon content by a factor of 4.5 in comparison to the anticipated 3:4 ratio. This indicates that the grinding and heating process with nc-FeS_2 may have resulted in alterations to the PTI surface, although this phenomenon has not been previously observed in the case of V_N-CN.[10] In all cases, the C 1s spectra exhibit two primary peaks associated with species of the aromatic system (Figure 8). The initial peak, which correlates with the N–C=N bond, is observed at 287.7 eV. The second peak, which is associated with C–C bonds, may be attributed to either adventitious carbon or graphitic carbon domains. It is observed at 284.8 eV.[37–39] Moreover, the π→π* satellite at 292.8 eV is clearly discernible in the spectra of 10 wt% nc-FeS_2

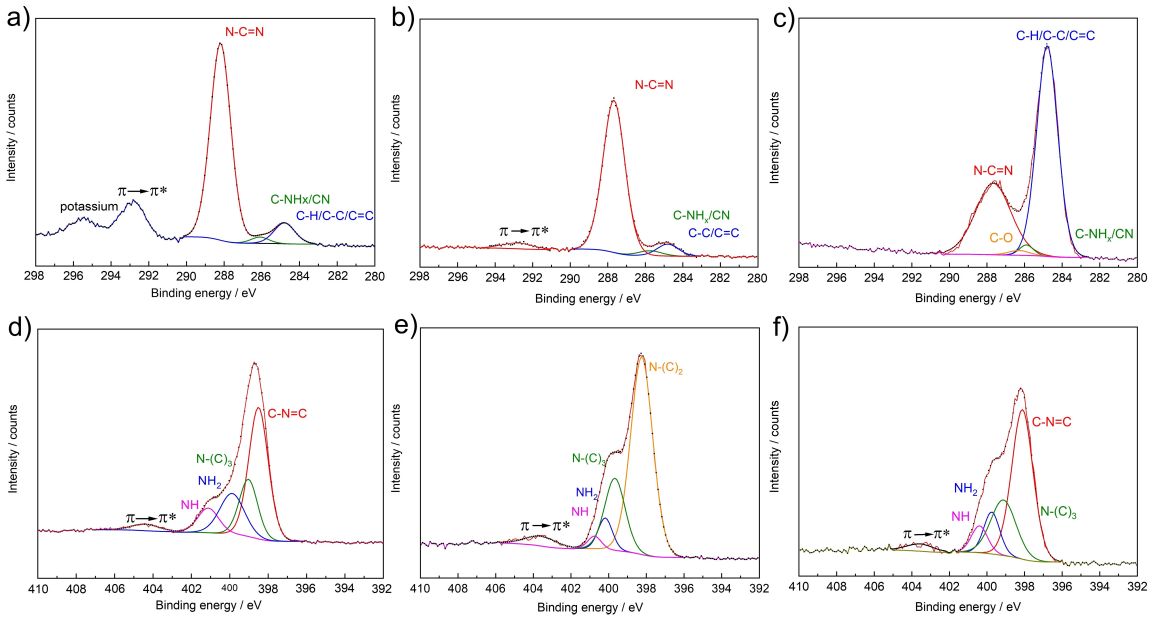

Figure 8. C 1s spectra for 10 wt% nc-FeS_2 on V_N-CN a), PTI b), and 10 wt% nc-FeS_2 on PTI c). Possible fitting of the N 1s spectra for 10 wt% nc-FeS_2 on V_N-CN d), PTI e), and 10 wt% nc-FeS_2 on PTI f) with the respective assignments of the various bindings.

on V_N-CN and PTI, whereas this satellite is absent in the spectra of 10 wt% nc-FeS_2 on PTI. This phenomenon may be attributed to a reduction in the number of free electrons present in the vacancies of PTI.[10] A further significant distinction between the V_N-CN composite and the PTI composite is the presence of a markedly elevated quantity of C–H/C–C/C=C bonds subsequent to composite formation (Figure 8c). This finding is in accordance with the previously mentioned observation of an increased number of carbon atoms in the PTI composite sample. Furthermore, it is anticipated that C–NH_x/C–N bonds will exhibit slightly elevated binding energies in comparison to carbon bonds, exhibiting a degree of overlap with the C–C/C=C and N–C=N peaks at approximately 285.8 eV. The interpretation and assignment of the N 1s spectra for materials similar to carbon nitride is still a matter of debate.[28,37,38,40] It is typically the case that fully condensed carbon nitride structures lack hydrogen bonds. However, the structure proposed by Pauly et al.[17] includes hydrogen, which suggests the presence of N–H bonds. The most prominent peak at 398.3 eV is predominantly ascribed to the C–N=C bond within the triazine moiety. A smaller peak at 403.6 eV is attributed to the $\pi \rightarrow \pi^*$ satellite. The peak at approximately 400 eV can be deconvoluted into three peaks: N–$(C)_3$ at 399.3 eV, NH_2 at 400.2 eV, and NH at 400.8 eV (Figure 8e). Additionally, a cyano group would be expected to appear at approximately 400 eV, however, this signal could not be identified due to overlapping signals.[38]

Photocatalytic HER Generation and Stability Investigation

The photocatalysis was carried out in a semi-batch setup in an argon atmosphere using 10 vol% methanol as a hole scavenger (Figure 9). The photocatalytic hydrogen evolution rates over time are shown, with an initial activation period leading to steady-state hydrogen evolution rates after several hours. After 7.5 hours of irradiation, the solution was filtered and analysed for NH3 from photocorrosion using ion chromatography.

The individual HER activities of the pure carbon nitride materials are lower than those of the corresponding composites, with values of 68 μmol/h for V_N-CN and 31 μmol/h for PTI. The activity of pure FeS_2 also varies depending on the precursor. Specifically, nc-FeS_2 shows an activity of 116 μmol/h after 7.5 hours, while nf-FeS_2 shows an activity of 51 μmol/h (cf. Table S3).

The incorporation of carbon nitrides into composites with FeS_2 generally results in an enhancement of the hydrogen evolution rate relative to that observed in the unmodified samples. In particular, a discernible co-catalyst effect is evident in the case of the nf-FeS_2 decorated PTI, which exhibits higher hydrogen evolution rates than both the individual materials combined. Accordingly, an illustrative experiment was conducted utilising 5 wt% nf-FeS_2 on PTI to ascertain the quantity of hydrogen produced (Figure S9). The sample was subjected to irradiation for a period of two hours, followed by an additional hour during which the lamp was deactivated. A linear increase in hydrogen production was observed throughout the course of the experiment, with each light period yielding a consistent outcome. As previously indicated in the aforementioned rates, the photocatalysis necessitates a period of stabilisation prior to attaining its ultimate production rate.

A comparable trend is observed across all composites, with 10 wt% FeS_2 demonstrating the highest level of activity, followed by 5 wt% and then 1 wt% FeS_2 in descending order. The composites of V_N-CN with nc-FeS_2 exhibit an enhanced hydrogen evolution reaction (HER) at the outset, which is likely attributable to the elimination of residual organic matter. In contrast, PTI with nc-FeS_2 exhibits a less pronounced initial increase in HER, which may be attributed to the enhanced stability of the PTI.

In our previous research on V_N-CN, we conducted photocatalytic measurements in argon and nitrogen, which yielded identical results in terms of ammonia formation. This finding substantiates the photocorrosion of the V_N-CN. It can therefore be concluded that V_N-CN is not an optimal photoabsorber for photocatalysis. In the same study, commercially available pyrite was employed as a co-catalyst.[10]

In order to categorise the instability of V_N-CN, PTI is employed as an alternative photoabsorber in the present study. The objective of the study was to identify the lowest possible level of ammonia resulting from photocorrosion. As illustrated in Figure 10, PTI exhibits minimal ammonia formation in an argon atmosphere. The distinct structure of PTI results in significantly higher stability, as evidenced by its NH_4^+ formation of 82 μg/L, which is much lower than that of other materials. This leads to a notable reduction in ammonia generation. This

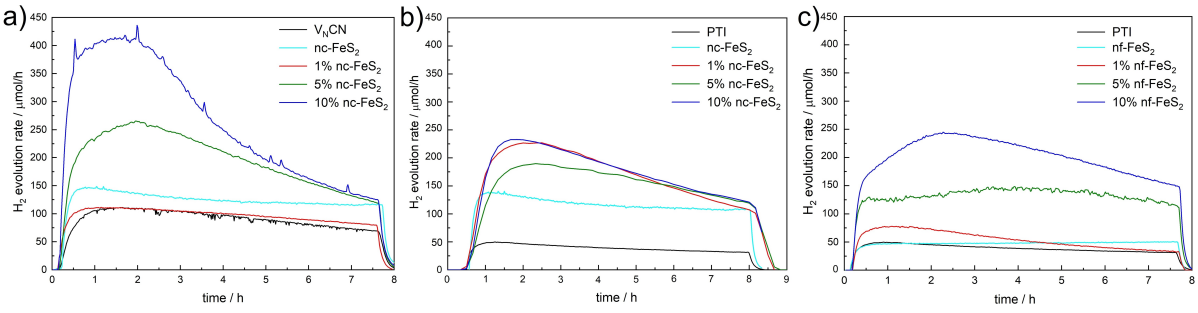

Figure 9. Photocatalytic hydrogen evolution rates of bare V_N-CN and the composites with 1, 5 and 10 wt% nc-FeS_2 a), the PTI and the composites with 1, 5 and 10 wt% nc-FeS_2 b), and PTI with 1, 5 and 10 wt% nf-FeS_2 c) in aqueous methanol (10 vol%) solution with 7.5 hours illumination time of a 350 W Hg lamp.

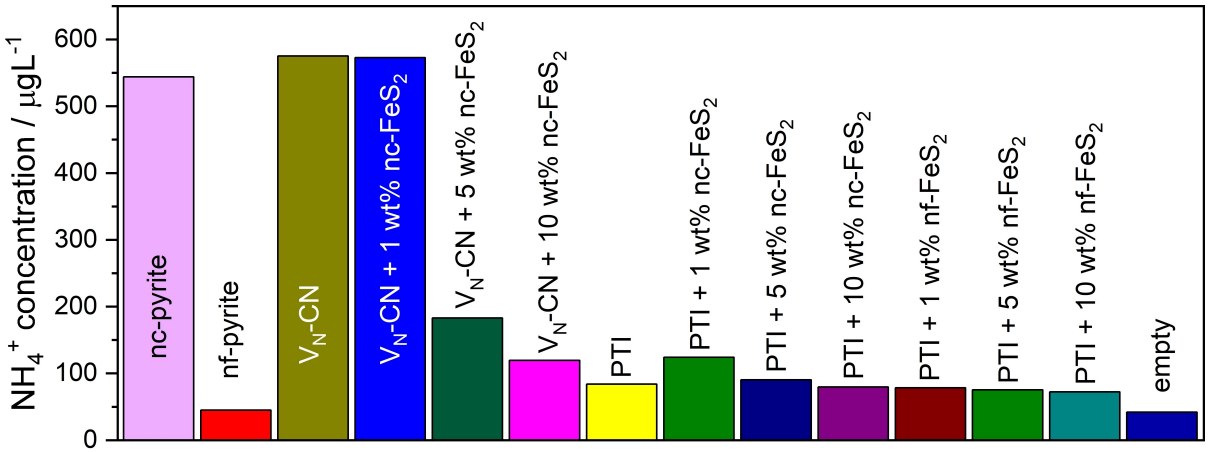

Figure 10. Ion chromatography measurements of NH_4^+ ions after the photocatalysis with the indicated samples.

could also be influenced by the fact that the synthesis was performed in vacuum. In contrast, pure V_N-CN exhibited an NH_4^+ formation of 575 µg/L, thereby confirming its strong photocorrosion instability, as had been previously reported. It is also possible that melamine residues in its structure may have contributed to ammonia formation. The enhanced stability of PTI is presumably attributable to its crystalline characteristics.

These findings have significant implications for potential applications of the photocatalytic nitrogen reduction reaction (NRR). Even when exposed to an argon atmosphere, the two CN materials exhibit markedly disparate photocorrosion behaviour. PTI displays enhanced stability as a semiconductor under irradiation, producing significantly less ammonia than the other material. In contrast, V_N-CN produced a considerable quantity of ammonia under light irradiation in an argon atmosphere, which could be erroneously interpreted as NRR when performed in a nitrogen atmosphere. To circumvent such erroneous outcomes, PTI is the superior option as an absorber material.

Two distinct synthesis methods for FeS_2 were conducted in the present study to assess the significance of the precursor choice in addressing analogous false-positive results for NRR. Furthermore, composites comprising PTI and V_N-CN were examined for their susceptibility to photocorrosion.

The preparation of FeS_2 with thiourea (nc-FeS_2) demonstrated a high ammonia value of 544 µg/L after 7.5 hours of light irradiation in argon. This is particularly notable given the absence of nitrogen as a carrier gas or reactant. It can be posited that the only possible explanation for this value is the presence of nitrogen-containing residues derived from the synthesis of thiourea. It is of concern that such nitrogen impurities could not be identified by XPS prior to this study (Figure 7). However, they still manifest as ammonia under light irradiation. In contrast, FeS_2 prepared from $Na_2S_2O_3$ (nf-FeS_2) exhibited minimal ammonia formation upon light irradiation (Figure 10), likely due to the absence of nitrogen-containing chemicals during the synthesis.

The examples of VN-CN and nc-FeS_2 demonstrate that the presence of impurities in nitrogen-containing precursors can result in erroneous positive results for NRR if not initially identified in argon. In the event that residual quantities of these substances are present within the material, the measured ammonia will effectively represent the degradation of the precursor. It is of paramount importance to consider this when preparing catalysts for NRR, where nitrogen-containing precursors or chemicals are used, but may be below the level of detection in techniques such as XPS.

The generation of NH_4^+ by composites of V_N-CN/nc-FeS_2 was found to decrease with increasing FeS_2 content, indicating an improvement in composite stability. This is evident from the fact that V_N-CN and nc-FeS_2 alone produce higher NH_4^+ levels than composites containing, for example, 10 wt% nc-FeS_2 on V_N-CN, which gives a result of 126 µg/L. The combination of 10 wt% nc-FeS_2 with the other components resulted in a slight reduction in ammonia generation, with a concentration of 80 µg/L. This discrepancy can be attributed to measurement inaccuracy rather than an improvement in stability. Nevertheless, the composites also appear to be unsuitable for potential NRR applications. Conversely, it would appear that nc-FeS_2 is stabilised by PTI. This is demonstrated by the observation that a solution containing 1 wt% nc-FeS_2 exhibits a markedly elevated ammonia generation of 124 µg/L in comparison to pure PTI or a mixture of 1% nc-FeS_2 and 99% PTI, which would yield an ammonia generation of 82.7 µg/L.

The novel synthesis method for nf-FeS_2 was devised with the objective of preventing the generation of ammonia, thereby facilitating a more precise evaluation of the impact of FeS_2 on the composite. As anticipated, the nf-FeS_2 itself does not produce ammonia (Figure 10). Furthermore, composites of PTI and nf-FeS_2 exhibit minimal photocorrosion, indicating that both materials may be suitable for potential future applications in photocatalytic NRR.

Subsequent to the photocatalytic experiments, the aforementioned materials, namely V_N-CN, PTI, nc-FeS_2 and nf-FeS_2, were subjected to additional characterisation. The post-photocatalytic XRD patterns of phase-pure V_N-CN, PTI, nc-FeS_2 and FeS_2 (Figure S10) still exhibit the same reflections.

Conclusions

Combinations of PTI with FeS_2 significantly increase the hydrogen evolution rates by more than three times compared to pure PTI, clearly indicating a co-catalytic effect. Using ion chromatography, we can confirm that PTI is much less photocorrosive than V_N-CN and can be used as a stable, low-cost absorber material for NRR in the future. Unfortunately, no NRR activity can be observed so far when PTI is decorated with nitrogen-free FeS_2 (not shown). In addition, we also show that the choice of precursors for the preparation of inorganic catalysts such as FeS_2 can lead to false positives in NRR, which needs to be more closely addressed by the community. The development of a nitrogen-free synthesis for FeS_2 produced very little ammonia under light irradiation, in stark contrast to FeS_2 synthesised using nitrogen-containing thiourea, which showed very high ammonia release in argon atmosphere. The only possible explanation for this effect remains nitrogen residues from the synthesis.

Experimental Section

Material synthesis and characterization: CN was prepared via thermal polymerization of melamine. 1 g of melamine (Sigma Aldrich, 99%) was calcined at 550 °C for 4 h in a closed crucible in air, using a heating ramp of 5 °C/min. The synthesis was repeated several times, and the powder was ground and thoroughly mixed. The vacancies were introduced by etching 2 g of the as-synthesized CN in 36 mL of 1 M KOH for 3 h under stirring. The material was collected via centrifugation and washed until neutral with ultrapure water. The product is referred to as V_N-CN.

The preparation of PTI/LiCl begins with weighing 17.6 mmol potassium chloride and 7.9 mmol melamine, and grinding until the mixture appears as a homogenous white powder. To this mixture 22 mmol of lithium chloride was added and ground together. This powder was then loaded into a reaction vessel that was approximately 10 inches long and a radius of 0.5 inches and sealed under vacuum. The reaction vessel was placed vertically into a muffle furnace and heated at a rate of 10 °C/min until 470 °C is reached. This temperature was held for 36 h, after which the furnace was cooled at a rate of 2 °C/h until the temperature reaches 350 °C. The furnace was then shut off and allowed to radiatively cool to room temperature. The heating rate, reaction time, and cooling rate were all optimized over course of numerous repeated experiments.[17] The product is repeatedly washed with de-ionized water to dissolve the excess salt and isolate the crystalline PTI/LiCl powder, which had a white to lightly beige color.

The nitrogen containing pyrite (nc-FeS_2) was synthesized by dissolving 1 mmol of $FeCl_3 \cdot 6H_2O$ (Grüssing, 99%) and 1 mmol thiourea (CH_4N_2S, Carl Roth, $\geq$99%) in 7.5 ml ethylene glycol (thermos scientific, 99.5%) respectively. Both solutions were mixed shortly before it was heated in the microwave for 15 minutes at 200 °C with a stirring speed of 800 rpm. The product was washed 3 times with EtOH (technical) and demineralized water with the sum of 30 mL and separated with the centrifuge.

The nitrogen free pyrite (nf-FeS_2) was obtained by dissolving 1 mmol of $FeCl_3 \cdot 6H_2O$ (Grüssing, 99%)) and 1 mmol $Na_2S_2O_3$ (Sigma Aldrich, 99%) in 7.5 ml ethylene glycol (thermos scientific, 99.5%) respectively. Both solutions were mixed shortly before it was heated in the microwave for 25 min at 200 °C with a stirring speed of 1000 rpm. The product was washed 5 times with EtOH (technical) and demineralized water with the sum of 30 mL and separated with the centrifuge.

For the V_N-CN composite formation the V_N-CN and the respective FeS_2 were ground for 10 min with a mortar, under addition of a low amount of i-propanol (p.a.). Subsequently the mixture was subjected to heat treatment for 2 h at 200 °C in air with a closed crucible, to improve interfacial contact.

The PTI composites were obtained similar to V_N-CN. PTI was ground with the respective FeS_2 for 10 min with a mortar, under addition of a low amount of i-propanol (p.a.). Subsequently the mixture was subjected to heat treatment for 2 h at 200 °C in air with a closed crucible, to improve interfacial contact.

The composites were analyzed before and after the photocatalytic experiments.

Powder X-ray diffraction (XRD) was measured on a Malvern PANalytical Empyrean device with Cu K_α irradiation ($\lambda_1 = 1.5406$ Å; $\lambda_2 = 1.54443$ Å). Acceleration voltage and emission current were set to 40 kV and 40 mA, respectively. Peak assignment was performed with X'Pert Highscore plus. The following PDF reference card was used for the reflection assignment in FeS_2: 00–042-1340.

Diffuse-reflectance UV/vis spectra were obtained using a Perkin Elmer Lambda 750 spectrometer with a Praying Mantis (Harrick) and spectralon as white standard. The Kubelka-Munk function[25] was used for the calculation of pseudo-absorption, f(R).

$$f(R) = \frac{(1-R)^2}{2 \cdot R}$$

For band gap determination, a Tauc Plot was used.[24]

$$[f(R) \cdot (h\nu)]^{\frac{1}{n}}$$

with n = 0.5 for direct band gaps and n = 2 for indirect ones.

For diffuse reflectance infrared Fourier transformed spectroscopy (DRIFT) a Bruker Alpha II spectrometer and the software OPUS were used. Sample scans were taken from 400–4000 cm^{-1}, with a resolution of 4 cm^{-1}.

Fluorescence measurements were conducted on a FluoTime 300 spectrometer from PicoQuant, with the software EasyTau2. Emission spectra were recorded at different excitation wavelengths from a 300 W Xe lamp at room temperature in air (Excitation wavelength: 355 nm). Time correlated single photon counting (TCSPC) spectra were measured using 355 nm laser excitation. The software EasyTau2 was employed for fitting decay curves. Using a tailfit with three exponentials, according to

$$Dec(t) = \sum_{i=1}^{n_{exp}} A_i e^{-\frac{t}{\tau_i}} + Bkgr_{Dec}$$

For steady-state measurements, the sample was positioned in a holder designed for solid powder specimens. For quantum yield (QY) measurements, a thin film was prepared on the inside of a cuvette. This cuvette was then placed in an integrating sphere. Measurements were performed in the "out" geometry configuration, where the film in the cuvette was placed outside the direct excitation path. To calculate the quantum yield, the intensity of the fluorescence emission was integrated. The area A_S was divided by the total integrated excitation intensity measured in an empty

reference cuvette (A_{BE}) minus the excitation intensity that was not absorbed by the sample A_{SE}

$$QY = \frac{A_S}{A_{BE} - A_{SE}}$$

X-ray photoelectron spectroscopy (XPS) was conducted using a Physical Electronics PHI VersaProbe III Scanning XPS Microprobe. The device utilized monochromatic Al K_α X-ray irradiation with a beam diameter of 100 μm, operating at a beam voltage of 15 kV and X-ray power of 25 W. The sample surface was pre-cleaned using argon cluster sputtering with a gas cluster ion beam. To mitigate surface charging, the samples were continuously flooded with slow-moving electrons and Ar+ ions. For survey scans, the pass energy was set to 224 eV and the step size to 0.4 eV.

Scanning electron microscopy (SEM) images were acquired using a Zeiss Leo 1530 device with an acceleration voltage of 2 and 3 kV, following sputter-coating with platinum. Energy dispersive X-ray spectroscopy (EDX) measurements were performed on the same instrument, utilizing an acceleration voltage of 20 kV.

Photocatalysis: The light-induced hydrogen evolution reaction (HER) was conducted in a semi-batch setup using a 700 W mercury immersion lamp, operated at 350 W, placed within a water-cooled quartz-glass inlay. For this experiment, 200 mg of the photocatalyst was dispersed in approximately 30 mL of ultrapure water via ultrasonic treatment for 10 min. This dispersion was then transferred to a glass reactor and diluted with ultrapure water and methanol to a final volume of 600 mL, with methanol comprising 10 vol%. Argon was used as the carrier gas, bubbled through at a flow rate of 100 mL min^{-1}. The reactor was degassed with argon overnight, approximately 14 hours, to remove any residual air. To eliminate nitrogen impurities, the argon gas was passed through a purification line containing 0.1 M $KMnO_4$ solution, followed by 0.1 M KOH. The dispersion was illuminated with 350 W for 7.5 hours, with the cooling liquid maintained at 10 °C to ensure conditions near standard temperature. A Lauda Proline RP845 cryostat was used for temperature control.

Evolving gases were passed through a drying rod and analyzed using a mass spectrometer (HPS-20 Q/, Hidden Analytical). After the reaction, the dispersion was immediately filtered and tested for NH_4^+ using ion chromatography.

Ion chromatography was used to analyze the reaction solution ammonia and nitrate by-products. The reaction solution was filtered with a 0.2 μm syringe filter. For the anions a dionex Aquion system from Thermo Fisher, equipped with a Dionex IonPac AS9-HC column and IonPac AG9-HC guard column was used for the analysis. 1×10^{-3} M $NaHCO_3$/8×10^{-3} M Na_2CO_3 was used as eluent, a UV detector was employed for quantification at a wavelength of 207 nm.

For cations a Dionex Aquion system from Thermo Fisher, equipped with a Dionex IonPac CS16 analytical column, a CG16 guard column, a CERS suppressor, and an electrical conductivity detector, was employed. A 30×10^{-3} M methanesulfonic acid solution was used as the eluent. A Dionex Aquion system from Thermo Fisher, equipped with a Dionex IonPac AS9-HC analytical column and an IonPac AG9-HC guard column, was used for the analysis. A 1×10^{-3} M $NaHCO_3$/8×10^{-3} M Na_2CO_3 solution served as the eluent, and quantification was performed using a UV detector at a wavelength of 207 nm.

Transmission electron microscopy (TEM) was conducted for the determination of sample size, and morphology using a 200 kV JEOL JEM-2200FS EFTEM, equipped with a Schottky FEG and an omega in-column energy filter. For the evaluation of the lattice planes ImageJ was used. Prior to the measurements small amounts of the powders were dispersed in ethanol (p.a.) via ultrasonification and drop casted onto the copper grid.

Acknowledgements

The authors would like to thank Mirco Ade and Kevin Ries for SEM/EDX measurements, Jonas Jungmann for TEM measurements, and Lion Schumacher for XPS measurements (all from University of Bayreuth). Moreover, we thank the Bavarian Polymer Institute (BPI) for usage of the XPS and SEM devices in the respective KeyLabs *Device Engineering* and *Electron Microscopy*. Research partially supported as part of the Center for Hybrid Approaches in Solar Energy to Liquid Fuels (CHASE), an Energy Innovation Hub funded by the U.S. Department of Energy, Office of Science, Office of Basic Energy Sciences under Award Number DE-SC0021173 (synthesis of PTI-LiCl). R.M. and J.K. acknowledge funding by the Deutsche Forschungsgemeinschaft (DFG, German Research Foundation) in the Priority Program 2370 "Nitroconversion" (project no. 501901537). Open Access funding enabled and organized by Projekt DEAL.

Conflict of Interests

The authors declare no conflict of interest.

Data Availability Statement

The data that support the findings of this study are available from the corresponding author upon reasonable request.

Keywords: photocatalysis · hydrogen generation · carbon nitride · photocorrosion

[1] D. Lawrence, K. Vandecar, *Nat. Clim. Chang.* **2015**, *5*, 27–36.
[2] M. Asif, T. Muneer, *Renew. Sustain. Energy Rev.* **2007**, *11*, 1388–1413.
[3] T. Ahmad, D. Zhang, *Energy Rep.* **2020**, *6*, 1973–1991.
[4] M. Carmo, D. L. Fritz, J. Mergel, D. Stolten, *Int. J. Hydrogen Energy* **2013**, *38*, 4901–4934.
[5] S. E. Hosseini, M. A. Wahid, *Renew. Sustain. Energy Rev.* **2016**, *57*, 850–866.
[6] M. Younas, S. Shafique, A. Hafeez, F. Javed, F. Rehman, *Fuel* **2022**, *316*, 123317.
[7] J. Wen, J. Xie, X. Chen, X. Li, *Appl. Surf. Sci.* **2017**, *391*, 72–123.
[8] S. Wang, J. Zhan, K. Chen, A. Ali, L. Zeng, H. Zhao, W. Hu, L. Zhu, X. Xu, *ACS Sustain. Chem. Eng.* **2020**, *8*, 8214–8222.
[9] H. Wang, M. Li, H. Li, Q. Lu, Y. Zhang, S. Yao, *Mater. Des.* **2019**, *162*, 210–218.
[10] J. Zander, J. Timm, M. Weiss, R. Marschall, *Adv. Energy Mater.* **2022**, *12*, 2202403.
[11] J. G. Chen, R. M. Crooks, L. C. Seefeldt, K. L. Bren, R. Morris Bullock, M. Y. Darensbourg, P. L. Holland, B. Hoffman, M. J. Janik, A. K. Jones, et al., *Science (80−)*. **2018**, *360,* eaar6611.
[12] W. J. Ong, L. L. Tan, Y. H. Ng, S. T. Yong, S. P. Chai, *Chem. Rev.* **2016**, *116*, 7159–7329.
[13] S. Cao, J. Low, J. Yu, M. Jaroniec, *Adv. Mater.* **2015**, *27*, 2150–2176.
[14] A. Aliakbari, M. S. Ghamsari, M. R. Mozdianfard, *Opt. Mater. (Amst).* **2020**, *107*, 110036.

[15] V. Ramasamy, P. Murahari, N. R. Banapurmath, K. Ramesh, *Carbon Trends* **2021**, *5*, 100079.
[16] R. Jiang, W. Li, K. Zhu, W. Ye, G. Zhu, G. Jia, F. Xu, J. Wang, T. Tao, Y. Wang, et al., *J. Alloys Compd.* **2022**, *920*, 166045.
[17] M. Pauly, J. Kröger, V. Duppel, C. Murphey, J. Cahoon, B. V Lotsch, P. A. Maggard, *Chem. Sci.* **2022**, *13*, 3187–3193.
[18] T. Iwasaki, M. Aono, S. Nitta, H. Habuchi, T. Itoh, S. Nonomura, *Diam. Relat. Mater.* **1999**, *8*, 440–445.
[19] J. C. Sánchez-López, C. Donnet, F. Lefèbvre, C. Fernández-Ramos, A. Fernández, *J. Appl. Phys.* **2001**, *90*, 675–681.
[20] H. J. Li, B. W. Sun, L. Sui, D. J. Qian, M. Chen, *Phys. Chem. Chem. Phys.* **2015**, *17*, 3309–3315.
[21] Y. Cao, Y. Guan, Y. Zhang, T. Zhao, W. Ding, W. Hui, J. Wu, *J. Taiwan Inst. Chem. Eng.* **2023**, *150*, 105019.
[22] B. V. Lotsch, M. Döblinger, J. Sehnert, L. Seyfarth, J. Senker, O. Oeckler, W. Schnick, *Chem. - A Eur. J.* **2007**, *13*, 4969–4980.
[23] K. Y. Ma, R. Lefèvre, Q. Li, J. Lago, O. Blacque, W. Yang, F. O. von Rohr, *Chem. Sci.* **2021**, *12*, 13870–13877.
[24] J. Tauc, *Mat. Res. Bull.* **1968**, *3*, 37–46.
[25] P. Kubelka, F. Munk, *Z. Tech. Phys* **1931**, *265*, 593–601.
[26] G. Socrates, *Infrared and Raman Characteristic Group Frequencies: Tables and Charts*, **2004**.
[27] H. Yu, R. Shi, Y. Zhao, T. Bian, Y. Zhao, C. Zhou, G. I. N. Waterhouse, L. Wu, C. Tung, T. Zhang, *Adv. Mater.* **2017**, *29*, 1605148..
[28] Z. Sun, S. Wang, Q. Li, M. Lyu, T. Butburee, B. Luo, H. Wang, J. M. T. A. Fischer, C. Zhang, Z. Wu, et al., *Adv. Sustain. Syst.* **2017**, *1*, 1–9.
[29] N. Zhou, P. Qiu, H. Chen, F. Jiang, *J. Taiwan Inst. Chem. Eng.* **2018**, *83*, 99–106.
[30] M. Kim, S. Hwang, J. S. Yu, *J. Mater. Chem.* **2007**, *17*, 1656–1659.
[31] L. Heymann, B. Schiller, H. Noei, A. Stierle, C. Klinke, *ACS Omega* **2018**, *3*, 3892–3900.
[32] D. Das, D. Banerjee, D. Pahari, U. K. Ghorai, S. Sarkar, N. S. Das, K. K. Chattopadhyay, *J. Lumin.* **2017**, *185*, 155–165.
[33] Z. Guo, B. Li, Y. Zhang, Q. Zhao, J. Zhao, L. Li, L. Feng, M. Wang, X. Meng, G. Zuo, *ChemistrySelect* **2019**, *4*, 8178–8182.
[34] Z. Gan, Y. Shan, J. Chen, Q. Gui, Q. Zhang, S. Nie, X. Wu, *Nano Res.* **2016**, *9*, 1801–1812.
[35] B. Choudhury, K. K. Paul, D. Sanyal, A. Hazarika, P. K. Giri, *J. Phys. Chem. C* **2018**, *122*, 9209–9219.
[36] G. Zhang, G. Li, Z. A. Lan, L. Lin, A. Savateev, T. Heil, S. Zafeiratos, X. Wang, M. Antonietti, *Angew. Chem. - Int. Ed.* **2017**, *56*, 13445–13449.
[37] W. Wang, H. Zhang, S. Zhang, Y. Liu, G. Wang, C. Sun, H. Zhao, *Angew. Chem. - Int. Ed.* **2019**, *58*, 16644–16650.
[38] E. Alwin, W. Nowicki, R. Wojcieszak, M. Zieliński, M. Pietrowski, *Dalt. Trans.* **2020**, *49*, 12805–12813.
[39] C. Ronning, H. Feldermann, R. Merk, H. Hofsäss, P. Reinke, *Phys. Rev. B - Condens. Matter Mater. Phys.* **1998**, *58*, 2207–2215.
[40] Z. Sun, J. M. T. A. Fischer, Q. Li, J. Hu, Q. Tang, H. Wang, Z. Wu, M. Hankel, D. J. Searles, L. Wang, *Appl. Catal. B Environ.* **2017**, *216*, 146–155.

Manuscript received: October 5, 2024
Revised manuscript received: December 11, 2024
Accepted manuscript online: December 23, 2024
Version of record online: January 15, 2025